Fabrication of porous carbonate apatite granules using microfiber and its histological evaluations in rabbit calvarial bone defects

Kazuya Akita[1], **Naoyuki Fukuda**[1], **Kumiko Kamada**[1], **Keiko Kudoh**[1], **Naito Kurio**[1], **Kanji Tsuru**[2], **Kunio Ishikawa**[3], **Youji Miyamoto**[1]

[1]Department of Oral Surgery, Institute of Biomedical Sciences, Tokushima University Graduate School, 3-18-15 Kuramoto-cho, Tokushima 770-8504, Japan

[2]Section of Bioengineering, Fukuoka Dental College, 2-15-1 Tamura, Sawara-ku, Fukuoka 812-8582, Japan

[3]Department of Biomaterials, Faculty of Dental Science, Kyushu University, 3-1-1 Maidashi, Higashi-ku, Fukuoka 812-8582, Japan

Corresponding author: Youji Miyamoto

Tel: +81-88-633-7354; Fax: +81-88-633-7462,

E-mail: miyamoto@tokushima-u.ac.jp

Abstract

Carbonate apatite (CO_3Ap) granules are known to show good osteoconductivity and replaced to new bone. On the other hand, it is well known that a porous structure allows bone tissue to penetrate its pores, and the optimal pore size for bone ingrowth is dependent on the composition and structure of the scaffold material. Therefore, the aim of this study was to fabricate various porous CO_3Ap granules through a two-step dissolution-precipitation reaction using $CaSO_4$ as a precursor and 30-, 50-, 120-, and 205-μm diameter microfibers as porogen and to find the optimal pore size of CO_3Ap. Porous CO_3Ap granules were successfully fabricated with pore size 8.2-18.7% smaller than the size of the original fiber porogen. Two weeks after the reconstruction of rabbit calvarial bone defects using porous CO_3Ap granules, the largest amount of mature bone was seen to be formed inside the pores of CO_3Ap (120) [porous CO_3Ap granules made using 120-μm microfiber] followed by CO_3Ap (50) and CO_3Ap (30). At 4 and 8 weeks, no statistically significant difference was observed based on the pore size, even though largest amount of mature bone was formed in case of CO_3Ap (120). It is concluded, therefore, that the optimal pore size of the CO_3Ap is that of CO_3Ap (120), which is 85 μm.

Keywords: carbonate apatite, hydroxyapatite, bone substitute, optimal pore size, bone formation

INTRODUCTION

Bone apatite is not carbonate-free hydroxyapatite [HAp; $Ca_{10}(PO_4)_6(OH)_2$], but carbonate apatite [CO_3Ap; $Ca_{10-a}(PO_4)_{6-b}(CO_3)_c(OH)_{2-d}$], which contains 6 wt%–9 wt% carbonate in its apatitic structure.[1] Therefore, CO_3Ap has a potential to be an ideal artificial bone substitute. Unfortunately, CO_3Ap begins to decompose and liberates CO_2 at around 400 °C.[2, 3] Doi *et al.*[4] found that some CO_3 remains in the apatitic structure, when CO_3Ap powder with higher CO_3 content is sintered at 750 °C, even with limited mechanical strength. In addition to the decreased CO_3 content, the crystallinity of CO_3Ap fabricated using the sintering method is extremely high compared to that of bone apatite.

Recently, a new method was proposed to fabricate chemically pure, low crystalline CO_3Ap through a dissolution-precipitation reaction in disodium hydrogen phosphate (Na_2HPO_4) aqueous solution using chemically pure precursor blocks, such as calcium carbonate ($CaCO_3$),[5-11] dicalcium phosphate dihydrate ($CaHPO_4 \cdot 2H_2O$),[12, 13] alpha-tricalcium phosphate (α-$Ca_3(PO_4)_2$),[14-19] and calcium sulfate ($CaSO_4$).[20-23] Upon immersion of the precursor block into Na_2HPO_4 solution, its composition gradually transforms to CO_3Ap, while maintaining the macroscopic structure of the precursor. The low crystalline CO_3Ap thus fabricated was resorbed by osteoclasts and replaced with bone similar to an autograft.[24, 25] Furthermore, the CO_3Ap block was found to up-regulate differentiation of osteoblasts[26] and exhibited much higher osteoconductivity than HAp.[24] Multi-center clinical trials for sinus floor augmentation also confirmed replacement of CO_3Ap with bone.[27] In Japan, there were no artificial bone substitutes

which are allowed for use adjacent to dental implants. Based on the clinical trials, the CO_3Ap was approved as an artificial bone substitute that can be used in all dental and maxillofacial fields, including those adjacent to dental implants, in Japan as Cytrans Granules® (GC Corporation, Tokyo, Japan).

On the other hand, it is well known that not only composition but also the structure of the bone substitute are important factors governing the usefulness of the bone substitute. Porous bone substitutes allow bone tissues and blood vessels to penetrate the bone substitute easily, which leads to good osteoconductivity and quick replacement by bone.[19, 28] Furthermore, a porous surface improves mechanical interlocking between the bone substitutes and surrounding existing bone, providing a greater mechanical stability.[29, 30] Therefore, CO_3Ap granules with porous structures are expected to be an ideal bone substitute owing to the their tendency to promote bone formation. To maximize the advantages of porous structures, the pore sizes should be optimized. It is well known that optimal pore size varies based on the composition of the structure.[29, 31] The objective of this study, therefore, was to fabricate porous CO_3Ap granules with different pore sizes and find an optimal pore size for CO_3Ap bone substitute.

MATERIALS AND METHODS

Preparation of porous CO_3Ap granules with different pore size

For preparation of porous CO_3Ap granules, calcium sulfate hemihydrate ($CaSO_4 \cdot 1/2H_2O$; New Fuji Rock White GC Corporation) was used as the precursor. $CaSO_4 \cdot 1/2H_2O$ powder and microfibers, 30 μm (Bellcouple; DIO CHEMICALS,

Tokyo, Japan), 50 μm (22TI; DIO CHEMICALS), 120 μm (V3M; DIO CHEMICALS), and 205 μm (Silver Thread; Unitika, Tokyo, Japan) in diameter were mixed such that the weight of the microfibers would be 10% that of $CaSO_4 \cdot 1/2H_2O$. Next, water was added at a powder to liquid (P/L) ratio of 0.2 and allowed to set under 50 MPa for 30 min using a cold isostatic pressing machine (CIP-CPH50; NPa System, Saitama, Japan). After compacting and setting, the sample was heated at a rate of 0.13 °C/min to 700 °C, kept for 5 hour to burn out the microfibers in the sample, crushed with a mortar and pestle, and sieved such that the size of the granules was between 1.0 and 1.4 mm.

These granules were immersed in 1.0 mol/L sodium carbonate (Na_2CO_3; Wako Pure Chemical Industries, Tokyo, Japan) solution at 4 °C for 7 days, and they were washed with distilled water. Next, they were immersed in a 1.0 mol/L Na_2HPO_4 (Wako Pure Chemical Industries) solution at 120 °C for 14 days, washed again with distilled water, and dried at room temperature. The diameter of the microfiber used for preparation of the porous CO_3Ap granules is stated in parenthesis in the following sentences. For instance, CO_3Ap (50) indicates porous CO_3Ap granules made using microfibers 50 μm in diameter according to the maker's description, while CO_3Ap (D) means dense granules without microfiber.

Morphological observation and pore size measurement

Morphology of the granules was observed by scanning electron microscopy (SEM: JCM-5700; JEOL, Tokyo, Japan) at an accelerating voltage of 15 kV after gold-palladium coating using a magnetron sputtering machine (IB-3; EIKO Corporation,

Tokyo, Japan). Diameter of the microfibers and pore size of each granule were measured from the SEM images and mean and standard deviation (SD) were calculated using 6 samples.

Additionally, pore size distribution was measured by the mercury intrusion technique using an automated mercury porosimeter (Autopore Ⅳ 9520 porosimeter; Micromeritics, Norcross, United States). Measurement was done based on the assumption that the contact angle of the CO_3Ap and the surface tension were 130° and 485 dynes/cm, respectively.

Compositional analysis

For compositional analysis, the granules were ground to fine powder and characterized by X-ray diffraction (XRD) analysis and Fourier transform infrared spectroscopy (FT-IR). XRD patterns were recorded using a powder X-ray diffractometer (SmartLab; Rigaku Corporation, Tokyo, Japan) with CuKα radiation operated at 40 kV and 40 mA. Scanning range was 2θ of 20° to 40° (where θ is the Bragg angle) in a continuous mode. FT-IR spectra were recorded using an FT-IR spectrometer (FT/IR-6200; JASCO Corporation, Tokyo, Japan) by the KBr method. The XRD patterns of standard $CaSO_4$ (Wako Pure Chemical Industries), $CaCO_3$ (Wako Pure Chemical Industries), commercial sintered HAp (NEOBONE®; Aimedic MMT, Tokyo, Japan), and commercial dense CO_3Ap granules (Cytrans Granules®) were used for comparison. Additionally, the FT-IR spectra of NEOBONE® and Cytrans Granules® were also used for comparisons.

Animal experiments

All animal experiments conformed to the guidelines of the animal ethics committee of the Institute for Frontier Medical Sciences, Tokushima University. Experimental protocols were reviewed and approved by the Tokushima University Animal Studies Committee (Approval number: T29-126). Thirty male Japanese white rabbits (body weight 3.0-3.5 kg, SLC, Shizuoka, Japan) were used in this study. The rabbits were subjected to general anesthesia by intravenous injection of ketamine (10 mg/kg) and xylazine (3 mg/kg). After shaving and disinfecting the head with iodine, 2% lidocaine was administered as local anesthesia. A 5-cm-incision was made into the calvarial skin, and the skin and periosteum were elevated. Four 8-mm, critical-sized bone defects were created by trephination using trephine bur (Dentech, Tokyo, Japan) under sterile saline irrigation,[32] and then CO_3Ap (D), CO_3Ap (30), CO_3Ap (50), CO_3Ap (120), and CO_3Ap (205) were implanted at random. After implantation, the periosteum and skin flap were repositioned and sutured using 4–0 nylon sutures.

Micro-Computed Tomography (μ-CT)

The animals were euthanized using intravenous pentobarbital (120 mg/kg) and the calvarial bone was harvested 2, 4, and 8 weeks after implantation. The extirpated calvarial bone was scanned using micro-computed tomography (μ-CT: SkyScan1176; Bruker microCT, Kontich, Belgium) at source voltage and current of 50 kV and 500 μA, respectively. The image data were recreated using the software NRecon Reconstruction

(Bruker micro-CT). Bone formation in the defect including the specimens was observed.

Histological evaluation

Five samples in each group were fixed in 10% buffer formaldehyde for 7 days and dehydrated by immersing in graded ethanol solutions from 70% to 100%. Finally, the samples were embedded in methyl methacrylate. Sections were prepared for pathological analysis using a modified interlocked diamond saw (Exakt, Hamburg, Germany) and Villanueva Goldner stain was applied to all the sections. In this method, mature bone and woven bone were stained green and red, respectively. Three samples in each group were submitted for decalcification and routine histological processing, and embedded in paraffin blocks. Specimens were sectioned horizontally at a thickness of 4 μm and stained with hematoxylin and eosin. All specimens were observed using an all-in-one microscope (BZ-X700; KEYENCE, Osaka, Japan). To clarify the elongation of newly formed bone from both edges of the bone defect, the defect area was divided into three parts, i.e., central portion and both sides of peripheral portion. The number of CO_3Ap granules contacted with new bone was counted at the central portion. Also, the percentage of newly formed woven bone and mature bone in the defect was calculated using Image J software as the ratio of the area of woven or mature bone to the area of original defect created by trephination.[33, 34] Furthermore, the percentage of woven bone and mature bone occupied in the pore of granules was also calculated as the area of newly formed bone to the total pore area of each granule.

Statistical analysis

For statistical analysis, one-way factorial analysis of variance (ANOVA) and Fisher's least significant difference (LSD) post-hoc tests were performed using Kaleida Graph 4. Values are expressed as mean ± SD. A *p*-value of <0.05 was considered statistically significant.

RESULTS

Figure 1 shows the typical SEM images of (a) CO_3Ap (D), (b) CO_3Ap (30), (c) CO_3Ap (50), (d) CO_3Ap (120), and (e) CO_3Ap (205). It is evident from these images that porous CO_3Ap granules with different pore sizes were successfully fabricated.

Figure 2 summarizes the typical XRD patterns of the heated set gypsum (a) before and (b) after immersion in 1 mol/L Na_2CO_3, and (c) after immersion in 1 mol/L Na_2HPO_4 solution. XRD patterns of standard (d) $CaSO_4$, (e) $CaCO_3$, (f) CO_3Ap, and (g) HAp were also recorded to facilitate comparison. As shown in the figure, heated set gypsum granules were $CaSO_4$. After the $CaSO_4$ granules were immersed in 1 mol/L Na_2CO_3, their chemical composition became that of $CaCO_3$ through a dissolution-precipitation reaction. On the other hand, on immersion of $CaCO_3$ granules in 1 mol/L Na_2HPO_4 solution, their composition became that of CO_3Ap. The crystallinity of CO_3Ap was smaller when compared to sintered HAp (g). No difference was found based on the pore size (data not shown).

FT-IR spectra of (a) fabricated CO_3Ap, (b) standard HAp, and (c) standard CO_3Ap

are summarized in Figure 3. Peaks corresponding to CO_3 (▲) in CO_3Ap were observed for fabricated CO_3Ap and standard CO_3Ap, whereas no such peaks were observed for HAp. In the case of fabricated CO_3Ap, a small OH peak (△) was observed similar to that in case of HAp. Thus, CO_3Ap fabricated by this method contains a hydroxyl group.

Figures 4 and 5 summarize the pore size distribution. As shown in Figure 4, three different pores were observed for porous CO_3Ap regardless of pore size. The smallest pores, with a diameter of approximately 0.02 μm, are the ones inside the CO_3Ap crystals. The medium pores, approximately 1 μm in diameter, are those between the CO_3Ap crystals, while the large pores with a diameter of 20 μm or larger, are the pores made by a fibrous porogen. The larger pore size distribution may be understood more clearly in Figure 5, where the pore volume is plotted laniary against the pore diameter. The pore diameters of CO_3Ap (30), CO_3Ap (50), CO_3Ap (120), and CO_3Ap (205) were 21 μm, 33 μm, 85 μm, and 171 μm, respectively.

Table 1 summarizes the diameters of original microfiber and the diameters of pores in each preparation step as measured by SEM. The diameter of pores decreased in each preparation step. Pore size of $CaSO_4$ granules was reduced by approximately 5% of the original fibers' diameter. The reduction rates of pore size of $CaCO_3$ and CO_3Ap granules through the dissolution-precipitation reaction were from 1.2 to 5.9% and 2.5 to 6.7% as compared to that in the previous reaction steps. In total, 8.2 to 18.7% linear shrinkage was observed when compared with the diameter of the original fiber and pore of the CO_3Ap granules.

Figure 6 shows the typical μ-CT images of (a-c) CO_3Ap (D), (d-f) CO_3Ap (30),

(g-i) CO_3Ap (50), (j-l) CO_3Ap (120), and (m-o) CO_3Ap (205) at 2, 4, and 8 weeks after implantation. Pores were observed for all porous CO_3Ap granules up to at least 8 weeks after implantation. At 2 weeks after implantation, new bone was formed only at the periphery of the bone defect, which then gradually elongated from the peripheral area to the central area at 4 weeks after implantation. At 8 weeks after implantation, most of the CO_3Ap granules were contacted with new bone.

Figure 7 shows the typical histological images with Villanueva Goldner staining of (a-c) CO_3Ap (D), (d-f) CO_3Ap (30), (g-i) CO_3Ap (50), (j-l) CO_3Ap (120), and (m-o) CO_3Ap (205) at 2, 4, and 8 weeks after implantation. The formation of new bone was observed from both ends of the defect, and it matured with the progression of the implantation period. All CO_3Ap granules demonstrated good osteoconductivity, regardless of the pore size. No tissue penetration was observed inside the CO_3Ap (D) at any instance after the implantation, whereas connective tissue, including new bone, penetrated the pores of the CO_3Ap granules at as early as 2 weeks after implantation. New bone elongated from the existing bone, and some of CO_3Ap granules, which were located at the periphery of the bone defects, were contacted with new bone at 4 weeks after implantation. Figure 8 indicates the percentage of CO_3Ap granules contacted with new bone at central portion in the defect. The amount of new bone elongated to the central portion of the defect increased with time. At 8 weeks after implantation, approximately 70% of the CO_3Ap granules contacted with new bone. No differences were observed based on the pore sizes.

Figure 9 shows the higher-magnification histological images of Villanueva Goldner

staining of (a-c) CO_3Ap (30), (d-f) CO_3Ap (50), (g-i) CO_3Ap (120), and (j-l) CO_3Ap (205) at 2, 4, and 8 weeks after implantation. As early as 2 weeks after implantation, mature bone was observed in the pores of CO_3Ap (30), CO_3Ap (50), and CO_3Ap (120) even though the amount observed was small. In contrast, no mature bone was observed in the pores of CO_3Ap (205). At 4 weeks after implantation, new bone was observed in the pores of all porous CO_3Ap granules regardless of the pore size. The amount of mature bone in the pores of porous CO_3Ap granules increased at 8 weeks after implantation.

Figure 10 shows the histological images of hematoxylin and eosin staining of (a) CO_3Ap (30), (b) CO_3Ap (50), (c) CO_3Ap (120), and (d) CO_3Ap (205) at 2 weeks after implantation. CO_3Ap granules demonstrated excellent biocompatibility. In other words, no inflammatory cell infiltration and abscess formation were observed around the granules. Osteoblast-like cells arranged along the surface of pores, red blood cells, and capillaries were observed at the center of most of the pores in the CO_3Ap (30), CO_3Ap (50), and CO_3Ap (120) implantations. In contrast, fibrous tissues were mainly observed instead of osteoblasts-like cells and blood vessels in the pores in the case of CO_3Ap (205). The amounts of fibrous tissue in the pore of CO_3Ap (30), CO_3Ap (50), CO_3Ap (120), and CO_3Ap (205) were 8.6 ± 3.1, 20.1 ± 9.0, 32.8 ± 15.5, and 77.7 ± 15.8%, respectively.

Figure 11 summarizes the amounts of new woven bone (a) and mature bone (b) formed inside of CO_3Ap granules as a function of the pore size and implantation period. Basically, the similar results were observed for woven bone and mature bone.

Statistically larger ($p < 0.05$) amounts of woven bone and mature bone were observed in the pores of CO_3Ap (120) than in CO_3Ap (30) and CO_3Ap (205) at 2 weeks after implantation. Although the largest amount of bone was seen in CO_3Ap (120) at both 4 and 8 weeks after surgery, no statistically significant difference was observed based on the pore sizes considered in this study. As expected, no bone tissues were observed in CO_3Ap (D) even up to 8 weeks after implantation.

Figure 12 summarizes the amounts of new woven bone (a) and mature bone (b) formed in the bone defect. No statistical difference was observed based on the pore size. The amount of woven bone was larger at 4 weeks when compared to 2 weeks, and no further increase was observed at 8 weeks. In contrast, the amount of matured bone increased gradually and became approximately twice at 8 weeks when compared to the results of 4 weeks.

To evaluate the resorption of the granules, the areas of the remaining granules were measured using histological sections. Although the sizes of CO_3Ap (D), CO_3Ap (30), CO_3Ap (50), CO_3Ap (120), and CO_3Ap (205) in the bone defect decreased 6.6 ± 7.6, 2.3 ± 6.7, 1.4 ± 9.4, 12.0 ± 6.8, and 18.0 ± 3.2% from 2 to 8 weeks after implantation, respectively, no statistical difference was observed among all implantation periods. The pore sizes in the implanted granules showed an increasing tendency with time, however no statistical difference was observed among the periods.

DISCUSSION

Porous CO_3Ap granules were fabricated by two-step dissolution-precipitation

reaction using gypsum as a precursor and microfiber as a porogen. Gypsum was found to have at least two advantages as a precursor. First, is its self-setting ability. Set gypsum containing microfiber was fabricated at under 50 MPa pressure. This allows for a relatively high content of the microfiber in the precursor. The second advantage is its thermal stability, as a high temperature is required to burn out the microfiber. Gypsum transforms to CO_3Ap through a dissolution-precipitation reaction and both one-step and two-step dissolution-precipitation reaction can be used for this fabrication. In this study, the two-step method was chosen to eliminate the remaining sulphate in the CO_3Ap granules. In the case of the two-step dissolution-precipitation reaction, first, the $CaCO_3$ granules are fabricated from $CaSO_4$ in Na_2CO_3 solution. When $CaSO_4$ granules are immersed in an aqueous solution, they slightly dissolve and supply Ca^{2+} and SO_4^{2-} to the solution as shown in Equation (1). When the solution contains CO_3^{2-}, it is supersaturated with respect to $CaCO_3$ and thus, the $CaCO_3$ precipitates, as shown in Equation (2).[35]

$$CaSO_4 \rightarrow Ca^{2+} + SO_4^{2-} \quad (1)$$

$$Ca^{2+} + CO_3^{2-} \rightarrow CaCO_3 \quad (2)$$

Another dissolution-precipitation reaction was carried out in the same manner using $CaCO_3$ granules as precursors. When $CaCO_3$ granules are immersed in aqueous solution, they dissolve to release Ca^{2+} and CO_3^{2-} into the solution as shown in Equation (3). When the solution contains PO_4^{3-}, the solution is supersaturated with respect to CO_3Ap, and thus, CO_3Ap is precipitated, as shown in Equation (4).[1]

$$CaCO_3 \rightarrow Ca^{2+} + CO_3^{2-} \quad (3)$$

$$Ca^{2+} + PO_4^{3-} + CO_3^{2-} \rightarrow Ca_{10-a}(PO_4)_{6-b}(CO_3)_c(OH)_{2-d} \quad (4)$$

As a consequence, porous CO_3Ap granules were fabricated, with the pore size corresponding to that of the original microfiber (Figure 1), although the diameter of the pore was decreased in each step (Table 1). It should be noted that CO_3Ap granules fabricated in this study have a hydroxyl group in apatitic structure, in contrast to those fabricated till date (Figure 3). Although gypsum was used as a precursor, $CaCO_3$ is formed after the initial dissolution-precipitation reaction. Therefore, a key difference is the temperature of the second dissolution-precipitation reaction in which $CaCO_3$ transformed to CO_3Ap, maintaining the macroscopic structure. In this study, Na_2HPO_4 solution at 120 °C was used to shorten the reaction period instead of at 80 °C, which is the temperature mostly used for CO_3Ap fabrication. The carbonate content of fabricated porous CO_3Ap (4.2 wt%) was less than that of commercial CO_3Ap (11.9 wt%) because the carbonate content of CO_3Ap was seen to decrease with increase in treatment temperature.

The actual diameter of the created pores of CO_3Ap granules was observed to be less than the size of the original fiber used in this study (Table 1). It is reasonable to speculate that this phenomenon resulted from the following two processes. The first is the linear shrinkage of gypsum caused by heating at 700 °C to burn out the microfibers.[36] The other cause is the precipitation of newly formed $CaCO_3$ and/or CO_3Ap crystals on the surface of the created pores during the dissolution-precipitation reaction.[28, 35] The thickness of the precipitated CO_3Ap is generally constant per surface area of the pore, provided that the reaction conditions are the same. Therefore, its

influence on narrowing the pore becomes lesser as the diameter of the pore becomes larger. Thus, the reduction rate through the dissolution-precipitation reaction decreased as the pore size increased.

The histological results revealed that CO_3Ap granules fabricated through two-step dissolution-precipitation reaction using gypsum as a precursor demonstrate excellent tissue compatibility and osteoconductivity similar to other CO_3Ap, even though a detailed comparison has not been done in the present study. Therefore, presence of a hydroxyl group in apatitic structure may not be a major factor in determining the tissue compatibility and osteoconductivity.

At 2 weeks after implantation, a statistically significant difference ($p < 0.05$) was observed in the case of the new bone tissue penetration interior to the CO_3Ap granules based on pore size (Figures 6, 11). Larger amounts of both woven and mature bones ($p < 0.05$) were seen to be formed inside the pores of CO_3Ap (120) than in those of CO_3Ap (30) and CO_3Ap (205). Blood vessels and red blood cells were observed in addition to osteoblasts inside the pores of CO_3Ap (120), CO_3Ap (50), and CO_3Ap (30). In other words, Haversian-like structures were formed inside the CO_3Ap pores. Interestingly, in the case of CO_3Ap (205), the pores were filled with fibrous tissue, while no mature bone and a few blood vessels were observed. Based on these results, we can safely conclude that the optimal size of the CO_3Ap fabricated using $CaSO_4$ as a precursor is 85 μm.

The optimum pore size for bone infiltration has been debatable and is known to depend on biomaterials, such as titanium, calcium phosphate, and synthesized polymer.[29, 31]

Frosch *et al.*[37] investigated the effect of different pore sizes (300, 400, 500, 600, and 1000 μm) of porous cylindrical titanium channels on cultured human osteoblasts. It was reported that higher osteocalcin gene expression in human osteoblasts and a greater degree of matrix mineralization were found in titanium channels with a pore size of 600 μm than in those with pore sizes 300 and 1000 μm. Moreover, channels with a pore size of 600 μm allowed for much deeper and faster osteoblast ingrowth than those with other pore sizes (300, 400, 500, and 1000 μm). Taniguchi *et al.*[38] also reported that porous titanium implants of pore size 600 μm showed rapid bone ingrowth and high fixation ability in rabbit femur and tibia as compared to those with pore sizes of 300 and 900 μm. Hara *et al*.[39] implanted porous cylindrical titanium implants with four different pore sizes (500, 640, 800, and 1000 μm) into the distal femur of rabbits. They observed that there was no difference in bone ingrowth in the titanium implants with pore sizes 500, 640, and 800 μm; however, less bone ingrowth was observed in the case of implants with 1000-μm pore size. These results suggest that porous titanium implants with a pore size of about 600 μm are suitable for bone formation.

HAp and beta-tricalcium phosphate (β-TCP) are the representative calcium phosphates for bone substitutes. Chang *et al*.[40] reported bone ingrowth in the porous HAp implants with different pore sizes (50, 100, 300, and 500 μm) in the proximal tibia of rabbits and concluded that the 300-μm sized pores in the HAp implants were optimum. Kuboki *et al*.[41] reported that alkaline phosphatase activity and osteocalcin content were higher in the BMP-containing porous HAp blocks with a pore size of 300–400 μm than in those with different pore sizes (106-212, 212-300, 400-500, and

500-600 μm), when implanted subcutaneously in rats. Moreover, infiltration of capillaries was observed in the porous HAp blocks with pore sizes more than 300 μm. Klenke *et al*.[42] reported the effect of pore sizes in the ranges 40-70, 70-140, 140-210, and 210-280 μm on the vascularization and osseointegration of porous biphasic calcium phosphate, composed of 80% HAp and 20% β-TCP, that was implanted into cranial defects in mice. The functional capillary density in the pores was significantly higher in cases where the pore sizes exceeded 140 μm than in those with pore sizes less than 140 μm. The volume of newly formed bone deposited within the pores increased as the pore size increased up to 280 μm. Taking these reports into consideration, a pore size ranging from 300 to 400 μm seems to be optimal for porous HAp.

Diao *et al.*[43] reported that porous β-TCP scaffolds with 100-μm pore size achieved the highest percentage of new bone ingrowth compared to those with other pore sizes (250 and 400 μm) in calvarial defects of rats at 4 weeks. Interestingly, pores of both 250 and 400 μm were occupied by larger amount of fibrous tissue. Their results are the same with the results of this investigation. In other words, fibrous tissue occupied pores of CO_3Ap(205) even though other pores, CO_3Ap(30), CO_3Ap(50), and CO_3Ap(120) were occupied by bone. Diao *et al*. claimed this phenomenon was caused by cell-cell contact. In short, smaller pore size provides narrower space for colonization and increases the opportunities for cell-cell contact, which facilitates osteoblastic differentiation. Therefore, faster new bone formation was observed in 100 μm pores than those in larger pores. Galois *et al.*[44] performed a study to quantify the bone ingrowth and biodegradability of porous β-TCP cylinders with different pore size ranges (45-80,

80-140, 140-200, and 200-250 μm) in the femoral condyles of rabbits. The amount of newly formed bone was statistically smaller in cylinders with 45-80 μm pore size than that in cylinders with larger pore sizes. Based on these studies, it was suggested that the optimum pore size of β-TCP is around 100 μm, which is smaller than that of HAp.

There has been no report till date regarding the optimal pore size of CO_3Ap granules for bone formation. Our results in this study demonstrated that CO_3Ap (120) showed the largest new bone formation inside the pores during the early stage among various porous CO_3Ap granules. This result indicated that the optimal pore size of CO_3Ap was relatively smaller than HAp, which is almost a non-resorbable bone substitute, and similar to β-TCP, which is a resorbable bone substitute. And, CO_3Ap is known to exhibit much higher solubility than sintered HAp. [45, 46] Therefore, one of the factors to govern optimal pore size may biodegradability of calcium phosphates. Dissolution of calcium phosphate elevate calcium ion concentration, leading up-regulation of osteoblast function.[47, 48] González-Vázquez *et al*.[48] reported that a 10 mmol/L extracellular calcium concentration promotes chemotaxis, proliferation, and differentiation in rat bone marrow mesenchymal stromal cells.

Additionally, it was reported that CO_3Ap has an ability to promote osteoblastic differentiation of human bone marrow cells earlier than sintered HAp,[26] which might be one of the reasons of increased bone formation in the smaller pore of CO_3Ap in an early stage.

Clinically, one of the drawbacks of dense granular bone substitutes is postoperative migration,[49, 50] which may cause outflow of granules from the implantation site after

surgery and the collapse of the form reconstructed with the granules. The resulting shortage of granules can lead to insufficient new bone formation. It is essential that granules allow bone tissue to penetrate them and combine with bone in the early stage to prevent postoperative migration. The results obtained in this study demonstrated that new bone formation was observed in the pores of porous CO_3Ap granules as early as 2 weeks after implantation. This may lead to earlier material fixation because of the improvement of mechanical interlocking between the porous granules and the surrounding bone.[29, 30]

It is known that porous bioceramics with higher porosity promote bone formation when compare to dense materials.[51-53] However, in our study, no statistically significant difference was found for the total amount of new bone formed at the bone defect based on the absence and presence of pores and the pore sizes (Figure 12). Obviously, this is due to the limited volume of pores introduced in the CO_3Ap granules. The amount of pores in CO_3Ap granules was approximately 7.5%, which may be negligible for total bone formation. Therefore, highly porous CO_3Ap granules made up of 85 μm-sized pores may be ideal artificial bone substitutes.

CONCLUSION

In conclusion, porous CO_3Ap granules were fabricated through a two-step dissolution-precipitation reaction using gypsum granules as precursor and microfibers as porogen. The pore size could be regulated by the diameter of original fiber used. Furthermore, CO_3Ap (120) showed the most efficient bone formation inside the pores

among the various fabricated porous CO_3AP granules in the calvarial defects of rabbits in early stage. It suggested that porous CO_3Ap granules may be useful for bone substitute material as compared to dense CO_3Ap granules, and the optimal pore size of the CO_3Ap bone substitute was estimated to be approximately 85 μm.

ACKNOWLEDGEMENTS

This research was supported, in part, by AMED under Grant Number JP18im0502004, along with Grant-in-Aids for Scientific Research (B) 18H03002 from the Japanese Society for the Promotion of Science and Research.

REFERENCES

1. Ishikawa K, Matsuya S, Lin X, Lei Z, Yuasa T, Miyamoto Y. Fabrication of low crystalline B-type carbonate apatite block from low crystalline calcite block. J Ceram Soc Jpn 2010;118:341-344.
2. Rau JV, Cesaro SN, Ferro D, Barinov SM, Fadeeva IV. FTIR study of carbonate loss from carbonated apatites in the wide temperature range. J Biomed Mater Res B Appl Biomater 2004;71:441-447.
3. Landi E, Tampieri A, Celotti G, Vichi L, Sandri M. Influence of synthesis and sintering parameters on the characteristics of carbonate apatite. Biomaterials 2004;25:1763-1770.
4. Doi Y, Koda T, Wakamatsu N, Goto T, Kamemizu H, Moriwaki Y, *et al*. Influence of carbonate on sintering of apatites. J Dent Res 1993;72(9):1279-1284.
5. Ishikawa K. Bone substitute fabrication based on dissolution-precipitation reaction. Materials 2010;3:1138-1155.
6. Lee Y, Hahm YM, Matsuya S, Nakagawa M, Ishikawa K. Characterization of macroporous carbonate-substituted hydroxyapatite bodies prepared in different phosphate solutions. J Mater Sci 2007;42:7843-7849.
7. Zaman CT, Takeuchi A, Matsuya S, Zaman QHMS, Ishikawa K. Fabrication of B-type carbonate apatite blocks by the phosphorylation of free-molding gypsum-calcite composite. Dent Mater J 2008;27:710-715.

8. Daitou F, Maruta M, Kawachi G, Tsuru K, Matsuya S, Terada Y, *et al*. Fabrication of carbonate apatite block based on internal dissolution-precipitation reaction of dicalcium phosphate and calcium carbonate. Dent Mater J 2010;29:303-308.
9. Maruta M, Matsuya S, Nakamura S, Ishikawa K. Fabrication of low-crystalline carbonate apatite foam bone replacement based on phase transformation of calcite foam. Dent Mater J 2011;30:14-20.
10. Sunouchi K, Tsuru K, Maruta M, Kawachi G, Matsuya S, Terada Y, *et al*. Fabrication of solid and hollow carbonate apatite microspheres as bone substitutes using calcite microspheres as a precursor. Dent Mater J 2012;31:549-557.
11. Ishikawa K, Munar ML, Tsuru K, Miyamoto Y. Fabrication of carbonate apatite honeycomb and its tissue response. J Biomed Mater Res A 2019;107:1014-1020.
12. Tsuru K, Kanazawa M, Yoshimoto A, Nakashima Y, Ishikawa K. Fabrication of carbonate apatite block through a dissolution-precipitation reaction using calcium hydrogen phosphate dihydrate block as a precursor. Materials 2017;10:374.
13. Kanazawa M, Tsuru K, Fukuda N, Sakemi Y, Nakashima Y, Ishikawa K. Evaluation of carbonate apatite blocks fabricated from dicalcium phosphate dihydrate blocks for reconstruction of rabbit femoral and tibial defects. J Mater Sci: Mater Med 2017;28:85-96.
14. Wakae H, Takeuchi A, Udoh K, Matsuya S, Munar M, LeGeros RZ, *et al*. Fabrication of macroporous carbonate apatite foam by hydrothermal conversion of α-tricalcium phosphate in carbonate solutions. J Biomed Mater Res A 2008;87:957-963.

15. Takeuchi A, Munar ML, Wakae H, Maruta M, Matsuya S, Tsuru K, *et al*. Effect of temperature on crystallinity of carbonate apatite foam prepared from α-tricalcium phosphate by hydrothermal treatment. Biomed Mater Eng 2009;19:205-211.
16. Karashima S, Takeuchi A, Matsuya S, Udoh K, Koyano K, Ishikawa K. Fabrication of low-crystallinity hydroxyapatite foam based on the setting reaction of alpha-tricalcium phosphate foam. J Biomed Mater Res A 2009;88:628-633.
17. Sugiura Y, Tsuru K, Ishikawa K. Fabrication of carbonate apatite foam based on the setting reaction of α-tricalcium phosphate foam granules. Ceram Int 2016;42:204-210.
18. Arifta TI, Munar ML, Tsuru K, Ishikawa K. Fabrication of interconnected porous calcium-deficient hydroxyapatite using the setting reaction of α-tricalcium phosphate spherical granules. Ceram Int 2017;43:11149-11155.
19. Ishikawa K, Arifta TI, Hayashi K, Tsuru K. Fabrication and evaluation of interconnected porous carbonate apatite from alpha tricalcium phosphate spheres. J Biomed Mater Res B Appl Biomater 2019;107:269-277.
20. Lowmunkong R, Sohmura T, Takahashi J, Suzuki Y, Matsuya S, Ishikawa K. Transformation of 3DP gypsum model to HA by treating in ammonium phosphate solution. J Biomed Mater Res B App Biomater 2007;80:386-393.
21. Lowmunkong R, Sohmura T, Suzuki Y, Matsuya S, Ishikawa K. Fabrication of freeform bone-filling calcium phosphate ceramics by gypsum 3D printing method. J Biomed Mater Res B Appl Biomater 2009;90:531-539.

22. Nomura S, Tsuru K, Matsuya S, Takahashi I, Ishikawa K. Fabrication of carbonate apatite block from set gypsum based on dissolution-precipitation reaction in phosphate-carbonate mixed solution. Dent Mater J 2014;33:166-172.

23. Ayukawa Y, Suzuki Y, Koyano K, Ishikawa K, Tsuru K. Histological comparison in rats between carbonate apatite fabricated from gypsum and sintered hydroxyapatite on bone remodeling. Biomed Res Int 2015;2015:579541.

24. Fujisawa K, Akita K, Fukuda N, Kamada K, Kudoh T, Ohe G, *et al*. Compositional and histological comparison of carbonate apatite fabricated by dissolution–precipitation reaction and Bio-Oss®. J Mater Sci Mater Med 2018;29:121.

25. Fujioka-Kobayashi M, Tsuru K, Nagai H, Fujisawa K, Ohe G, Ishikawa K, *et al*. Fabrication and evaluation of carbonate apatite-coated calcium carbonate bone substitutes for bone tissue engineering. J Tissue Eng Regen Med 2018;12:2077-2087.

26. Nagai H, Kobayashi-Fujioka M, Fujisawa K, Ohe G, Takamaru N, Hara K, *et al*. Effects of low crystalline carbonate apatite on proliferation and osteoblastic differentiation of human bone marrow cells. J Mater Sci Mater Med. 2015;26:99-107.

27. Kudoh K, Fukuda N, Kasugai S, Koyano K, Matsushita Y, Ogino Y, *et al*. Maxillary sinus floor augmentation using low-crystalline carbonate apatite granules with simultaneous implant installation: First-in-human clinical trial. J Oral and Maxillofac Surg 2019;77:985e1-11.

28. Zhao YN, Fan JJ, Li ZQ, Liu YW, Wu YP, Liu J. Effects of Pore Size on the Osteoconductivity and Mechanical Properties of Calcium Phosphate Cement in a Rabbit Model. Artif Organs 2017;41:199-204.
29. Karageorgiou V, Kaplan D. Porosity of 3D biomaterial scaffolds and osteogenesis. Biomaterials 2005;26:5474-5491.
30. Hannink G, Arts JJ. Bioresorbability, porosity and mechanical strength of bone substitutes: what is optimal for bone regeneration?. Injury 2011;42:S22-S25.
31. Bobbert FSL, Zadpoor AA. Effects of bone substitute architecture and surface properties on cell response, angiogenesis, and structure of new bone. J Mater Chem B 2017;5:6157-6414.
32. Borie E, Fuentes R, del Sol F, Oporto G, Engelke W. The influence of FDBA and autogenous bone particles on regeneration of calvaria defects in the rabbit; A pilot study. Ann Anat 2011;193:412-417.
33. Abramoff MD, Magelhaes PJ, Ram SJ. Image Processing with ImageJ. Biophotonics International 2004;11:36-42.
34. Schneider CA, Rasband WS, Eliceiri KW. NIH Image to ImageJ: 25 years of image analysis. Nature Methods 2012;9:671-675.
35. Ishikawa K, Kawachi G, Tsuru K, Yoshimoto A. Fabrication of calcite blocks from gypsum blocks by compositional transformation based on dissolution-precipitation reactions in sodium carbonate solution. Materials Science and Engineering C 2017;72:389-393.

36. Ishikawa K, Tram NX, Tsuru K, Toita R. Fabrication of porous calcite using chopped nylon fiber and its evaluation using rats. J Mater Sci Mater Med 2015;26:94.

37. Frosch KH, Barvencik F, Viereck V, Lohmann CH, Dresing K, Breme J, *et al*. Growth behavior, matrix production, and gene expression of human osteoblasts in defined cylindrical titanium channels. J Biomed Mater Res A 2004;68:325-334.

38. Taniguchi N, Fujibayashi S, Takemoto M, Sasaki K, Otsuki B, Nakamura T, *et al*. Effect of pore size on bone ingrowth into porous titanium implants fabricated by additive manufacturing: An in vivo experiment. Materials Science and Engineering C 2016;59:690-701.

39. Hara D, Nakashima Y, Sato T, Hirata M, Kanazawa M, Kohno Y, *et al*. Bone bonding strength of diamond-structured porous titanium-alloy implants manufactured using the electron beam-melting technique. Mater Sci Eng C Mater Biol Appl 2016;59:1047-1052.

40. Chang BS, Lee CK, Hong KS, Youn HJ, Ryu HS, Chung SS, Park KW. Osteoconduction at porous hydroxyapatite with various pore configurations. Biomaterials 2000;21(12):1291-8.

41. Kuboki Y, Jin Q, Takita H. Geometry of carriers controlling phenotypic expression in BMP-induced osteogenesis and chondrogenesis. J Bone Joint Surg Am 2001;83:S105-15.

42. Klenke FM, Liu Y, Yuan H, Hunziker EB, Siebenrock KA, Hofstetter W. Impact of pore size on the vascularization and osseointegration of ceramic bone substitutes in vivo. J Biomed Mater Res A 2008;85:777-86.

43. Diao J, OuYang J, Deng T, Liu X, Feng Y, Zhao N, *et al*. 3D-Plotted Beta-Tricalcium Phosphate Scaffolds with Smaller Pore Sizes Improve In Vivo Bone Regeneration and Biomechanical Properties in a Critical-Sized Calvarial Defect Rat Model. Adv Healthc Mater 2018;1800441:1-9.

44. Galois L, Mainard D. Bone ingrowth into two porous ceramics with different pore sizes: an experimental study. Acta Orthop Belg 2004;70:598-603.

45. Mano T, Akita K, Fukuda N, Kamada K, Kurio N, Ishikawa N, Miyamoto Y. Histological comparison of three apatitic bone substitutes with different carbonate contents in alveolar bone defects in a beagle mandible with simultaneous implant installation. J Biomed Mater Res B Appl Biomater 2019;17:1-10.

46. Ishikawa N, Miyamoto Y, Tsuchiya A, Hayashi K, Tsuru K, Ohe G. Physical and Histological Comparison of Hydroxyapatite, Carbonate Apatite, and β-Tricalcium Phosphate Bone Substitutes. J Biomed Mater Res B Appl Biomater 2018;16:10.

47. Maeno S, Niki Y, Matsumoto H, Morioka H, Yatabe T, Funayama A, *et al*. The effect of calcium ion concentration on osteoblast viability, proliferation and differentiation in monolayer and 3D culture. Biomaterials 2005;26:4847-4855.

48. González-Vázquez A, Planell JA, Engel E. Extracellular calcium and CaSR drive osteoinduction in mesenchymal stromal cell. Acta Biomater 2014;10:2824-2833.

49. Wittkampf ARM. Fibrin Glue as Cement for HA-Granules. J Cranio Max Fac Surg 1989;17:179-181.

50. Kent JN, Quinn JH, Zide MF, Guerra LR, Boyne PJ. Alveolar Ridge Augmentation Using Nonresorbable Hydroxyapatite with or without Autogenous Cancellous Bone. J Oral Maxillofac Surg 1963;41:629-642.

51. Barba A, Maazouz Y, Diez-Escudero A, Rappe K, Espanol M, Montufar EB, *et al*. Osteogenesis by foamed and 3D-printed nanostructured calcium phosphate scaffolds: Effect of pore architecture. Acta Biomater 2018;79:135-147.

52. Zhou K, Yu P, Shi X, Ling T, Zeng W, Chen W, *et al*. Hierarchically Porous Hydroxyapatite Hybrid Scaffold Incorporated with Reduced Graphene Oxide for Rapid Bone Ingrowth and Repair. ACS Nano 2019;13:9595-9606.

53. Matsuda H, Takabatake K, Tsujigiwa H, Watanabe S, Ito S, Kawai H, *et al*. Effects of the Geometrical Structure of a Honeycomb TCP on Relationship between Bone / Cartilage Formation and Angiogenesis. Int J Med Sci 2018;15(14):1582-1590.

Figure captions

FIGURE 1. Typical SEM images of (a) CO_3Ap (D), (b) CO_3Ap (30), (c) CO_3Ap (50), (d) CO_3Ap (120), and (e) CO_3Ap (205).

FIGURE 2. Typical XRD patterns of the heated set gypsum (a) before immersion, (b) after immersion in 1 mol/L Na_2CO_3, (c) after immersion in 1 mol/L Na_2HPO_4 solution, (d) with $CaSO_4$, (e) with $CaCO_3$, (f) with commercial CO_3Ap (Cytrans Granules®), and (g) with commercial sintered HAp (NEOBONE®).

FIGURE 3. FT-IR spectra of (a) fabricated porous CO_3Ap, (b) commercial sintered HAp (NEOBONE®), and (c) commercial CO_3Ap (Cytrans Granules®). (▲:CO_3, △:OH)

FIGURE 4. Mercury intrusion porosimetry curves and pore distributions obtained for fabricated porous CO_3Ap granules.

FIGURE 5. Mercury intrusion porosimetry curves and large pore distributions obtained for fabricated porous CO_3Ap granules.

FIGURE 6. μ-CT images of (a, b, c) CO_3Ap (D), (d, e, f) CO_3Ap (30), (g, h, i) CO_3Ap (50), (j, k, l) CO_3Ap (120), and (m, n, o) CO_3Ap (205) at 2, 4, and 8 weeks after implantation.

FIGURE 7. Typical histological images with Villanueva Goldner staining of (a, b, c) CO_3Ap (D), (d, e, f) CO_3Ap (30), (g, h, i) CO_3Ap (50), (j, k, l) CO_3Ap (120), and (m, n, o) CO_3Ap (205) at 2, 4, and 8 weeks after implantation.

FIGURE 8. Percentage of the CO_3Ap granules contacted with new bone at central portion in the bone defect at 2, 4, and 8 weeks after implantation (n = 5) (*$p < 0.05$).

FIGURE 9. Typical higher-magnification histological images with Villanueva Goldner staining of (a, b, c) CO_3Ap (30), (d, e, f) CO_3Ap (50), (g, h, i) CO_3Ap (120), and (j, k, l) CO_3Ap (205) at 2, 4, and 8 weeks after implantation. (∗ : CO_3Ap granule)

FIGURE 10. Typical histological images with hematoxylin and eosin staining of (a) CO_3Ap (30), (b) CO_3Ap (50), (c) CO_3Ap (120), and (d) CO_3Ap (205) at 2 weeks after implantation. (Ob: osteoblast, V: blood vessel, F: fibrous tissue)

FIGURE 11. Percentage of new woven bone (a) and mature bone (b) in the pores of CO_3Ap granules at 2, 4, and 8 weeks after implantation (n = 5) (*$p < 0.05$, **$p < 0.01$).

FIGURE 12. Percentage of new woven bone (a) and mature bone (b) in the whole bone defects reconstructed by porous CO_3Ap at 2, 4, and 8 weeks after implantation (n = 5).

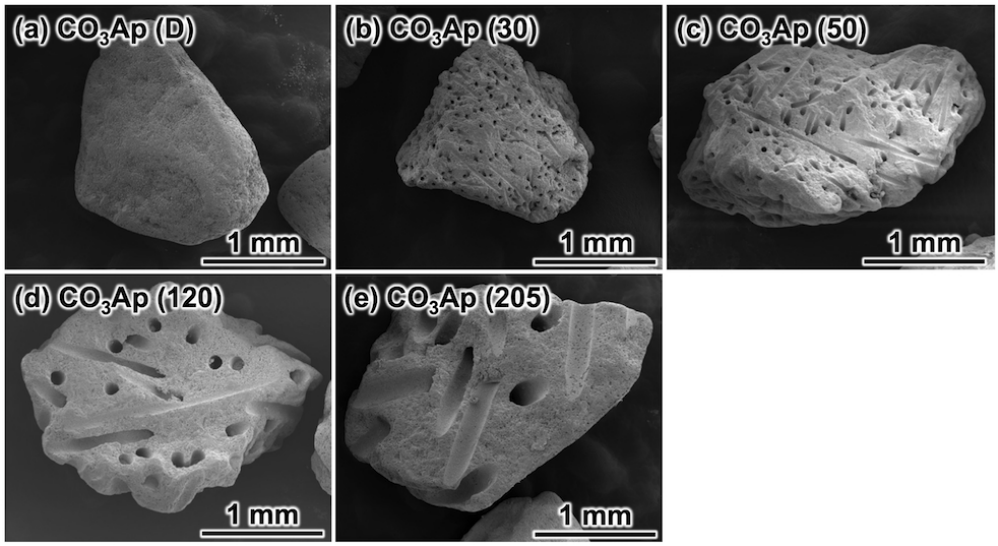

FIGURE 1. Typical SEM images of (a) CO_3Ap (D), (b) CO_3Ap (30), (c) CO_3Ap (50), (d) CO_3Ap (120), and (e) CO_3Ap (205).

833x455mm (30 x 30 DPI)

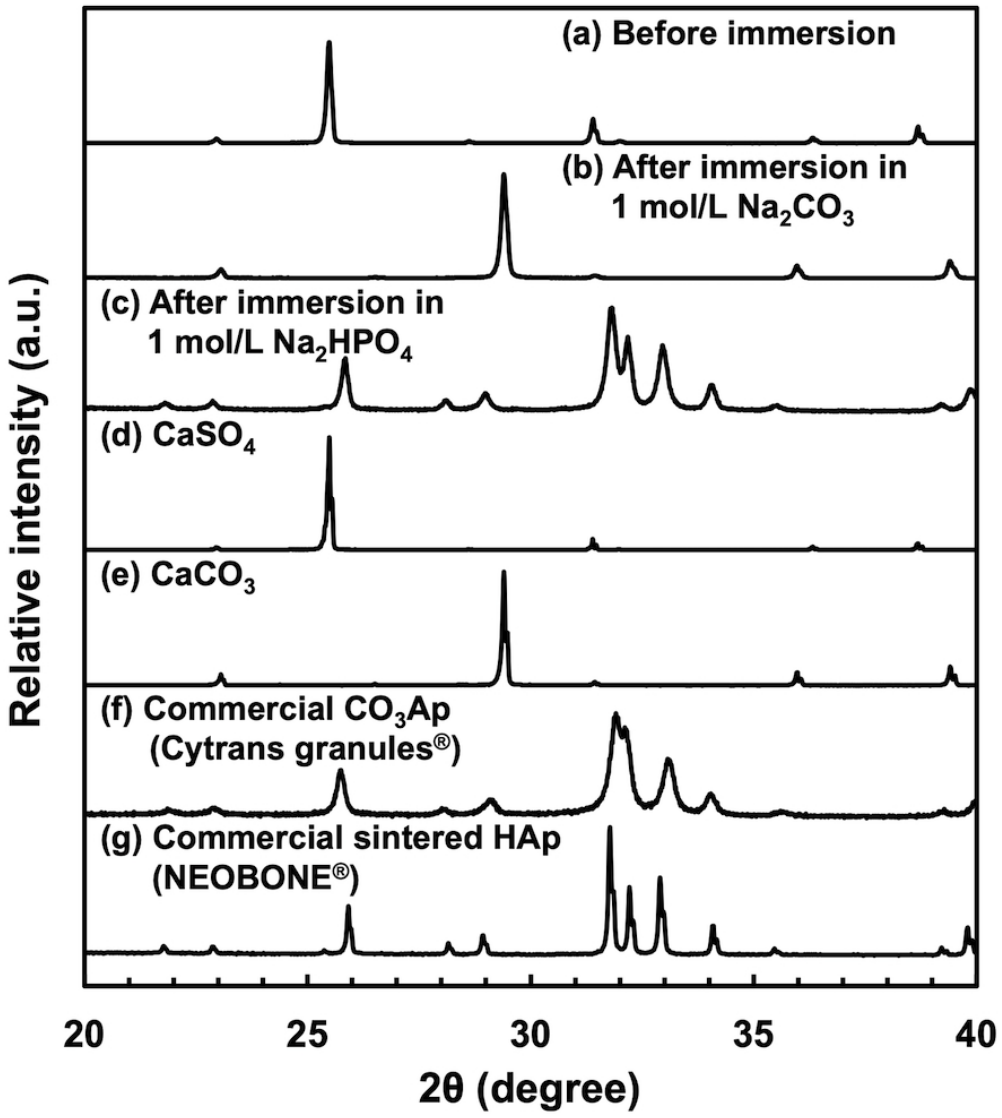

FIGURE 2. Typical XRD patterns of the heated set gypsum (a) before immersion, (b) after immersion in 1 mol/L Na_2CO_3, (c) after immersion in 1 mol/L Na_2HPO_4 solution, (d) with $CaSO_4$, (e) with $CaCO_3$, (f) with commercial CO_3Ap (Cytrans Granules®), and (g) with commercial sintered HAp (NEOBONE®).

561x626mm (40 x 40 DPI)

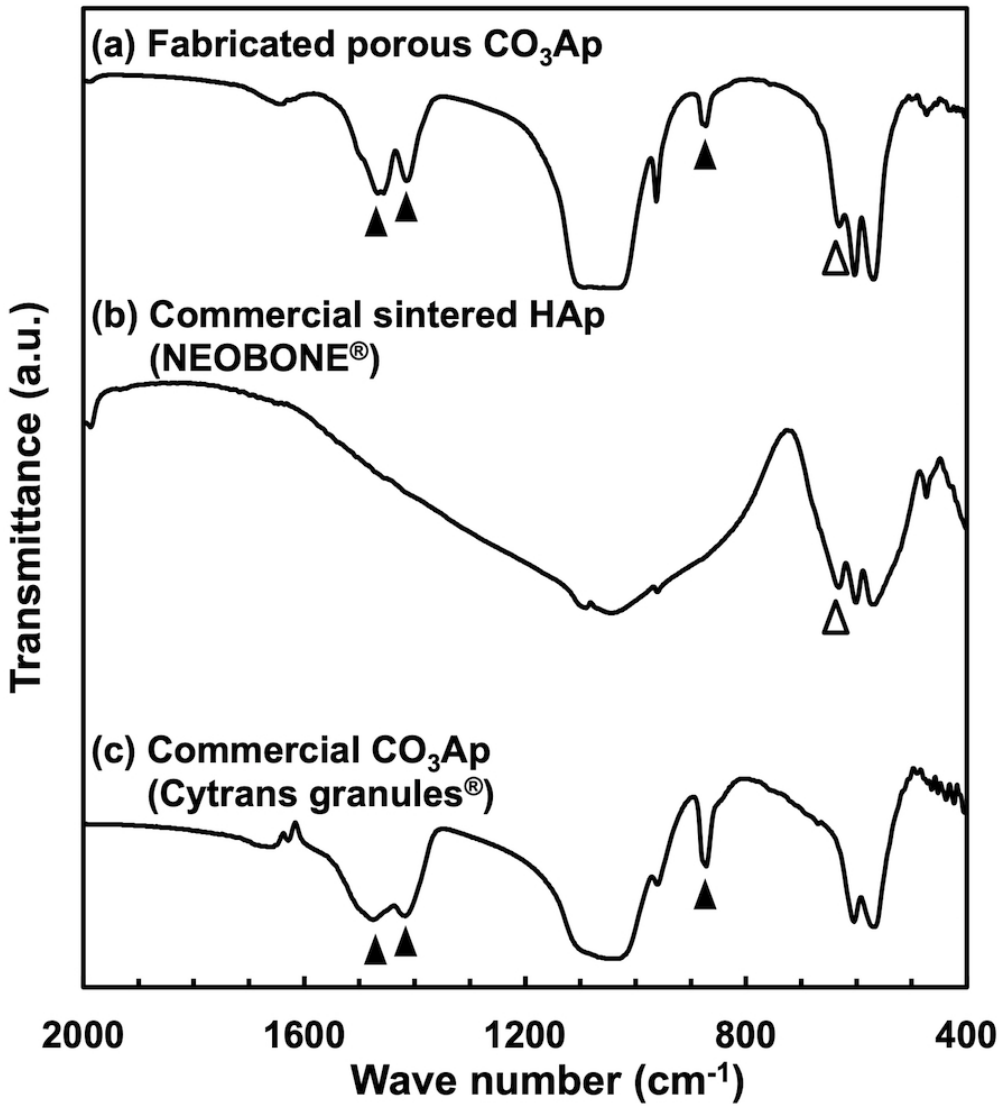

FIGURE 3. FT-IR spectra of (a) fabricated porous CO_3Ap, (b) commercial sintered HAp (NEOBONE®), and (c) commercial CO_3Ap (Cytrans Granules®). (▲:CO_3, △:OH)

566x627mm (40 x 40 DPI)

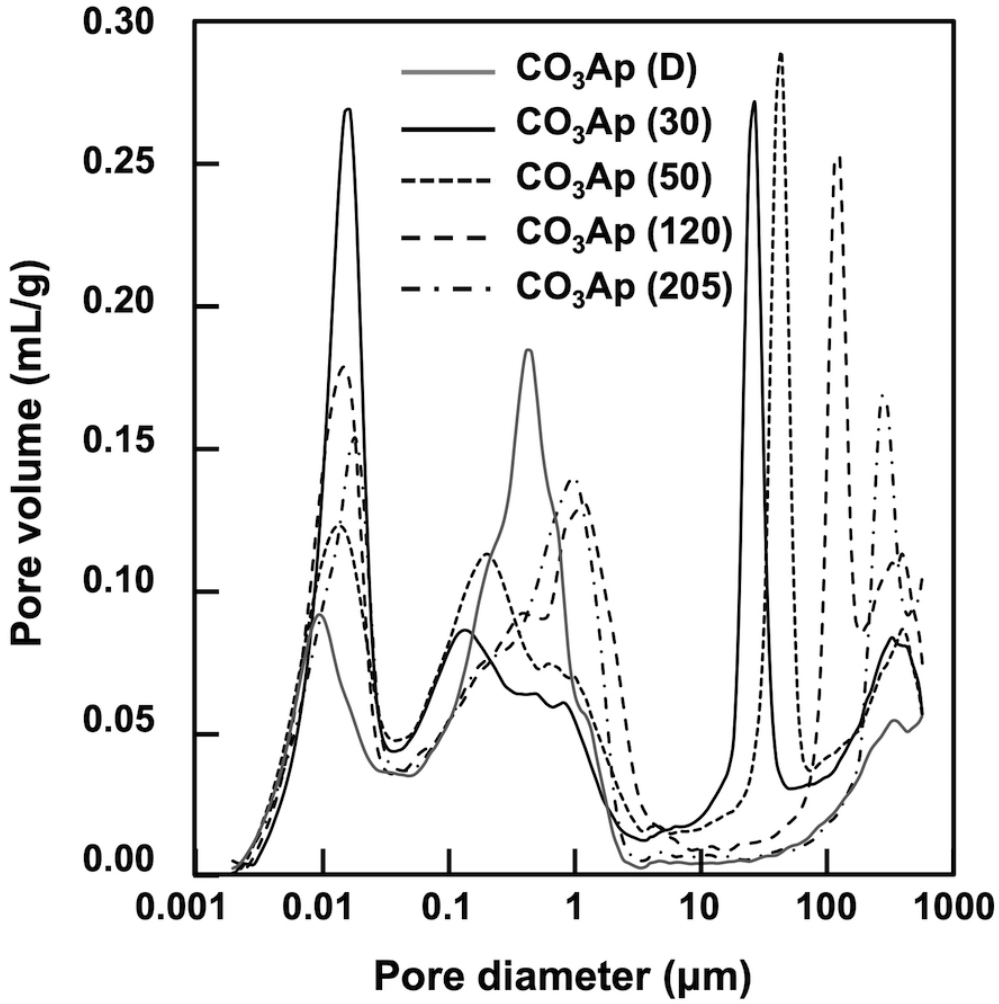

FIGURE 4. Mercury intrusion porosimetry curves and pore distributions obtained for fabricated porous CO_3Ap granules.

564x567mm (40 x 40 DPI)

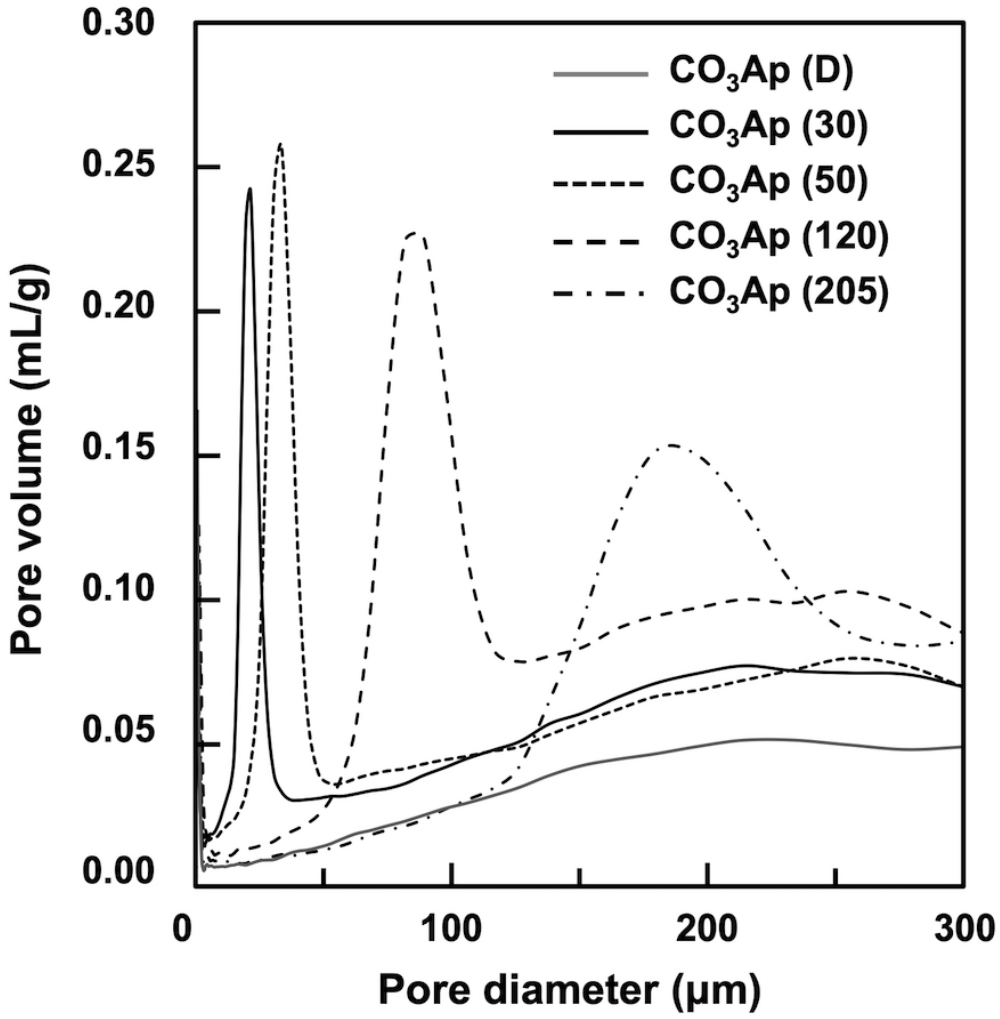

FIGURE 5. Mercury intrusion porosimetry curves and large pore distributions obtained for fabricated porous CO_3Ap granules.

556x567mm (40 x 40 DPI)

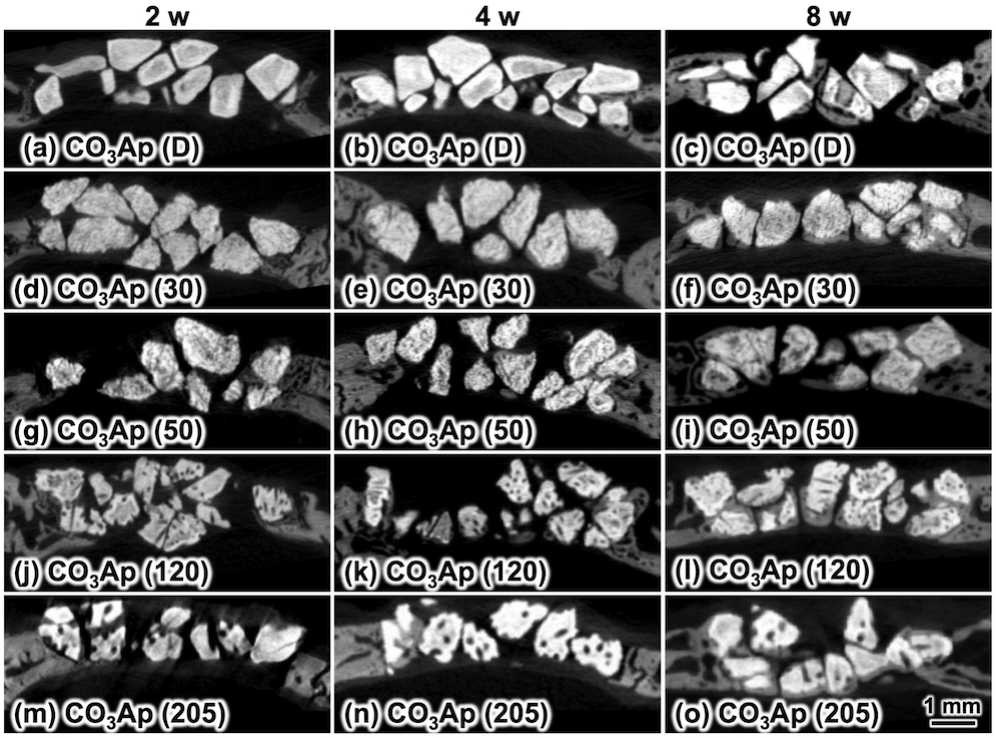

FIGURE 6. μ-CT images of (a, b, c) CO_3Ap (D), (d, e, f) CO_3Ap (30), (g, h, i) CO_3Ap (50), (j, k, l) CO_3Ap (120), and (m, n, o) CO_3Ap (205) at 2, 4, and 8 weeks after implantation.

844x623mm (30 x 30 DPI)

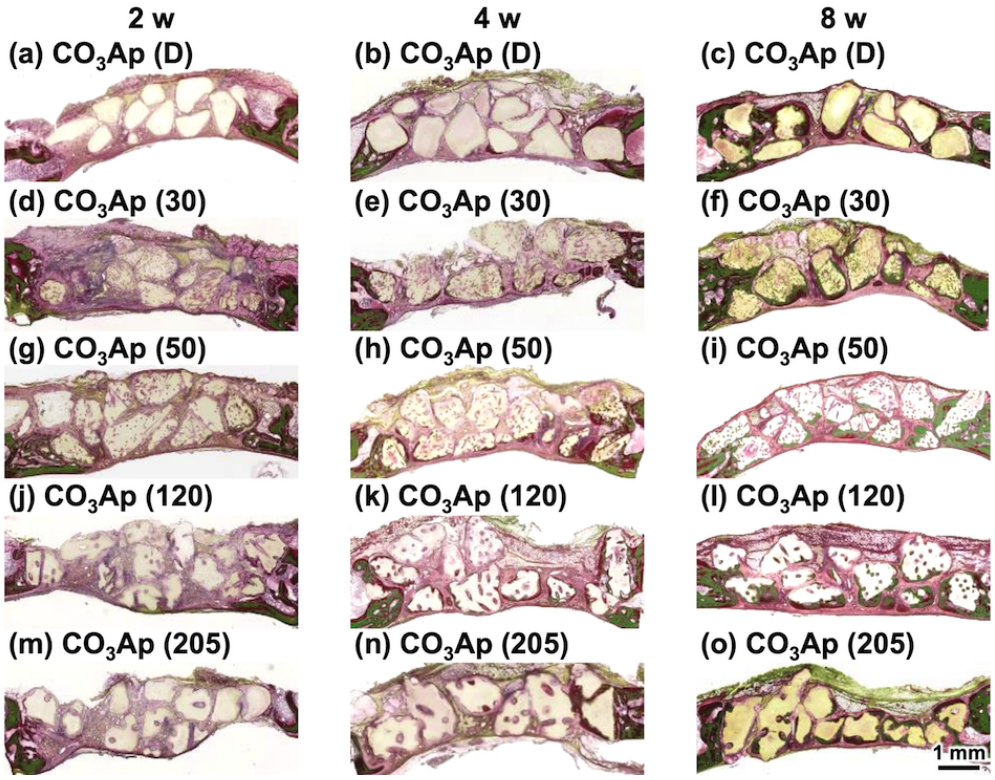

FIGURE 7. Typical histological images with Villanueva Goldner staining of (a, b, c) CO_3Ap (D), (d, e, f) CO_3Ap (30), (g, h, i) CO_3Ap (50), (j, k, l) CO_3Ap (120), and (m, n, o) CO_3Ap (205) at 2, 4, and 8 weeks after implantation.

807x623mm (30 x 30 DPI)

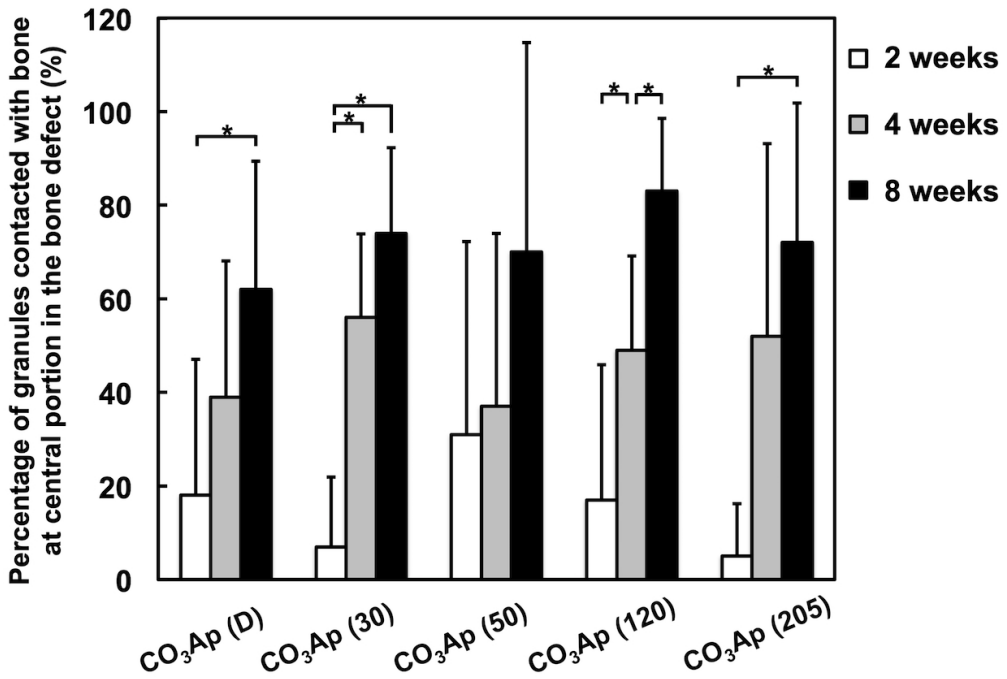

FIGURE 8. Percentage of the CO_3Ap granules contacted with new bone at central portion in the bone defect at 2, 4, and 8 weeks after implantation (n = 5) (*$p < 0.05$).

781x527mm (40 x 40 DPI)

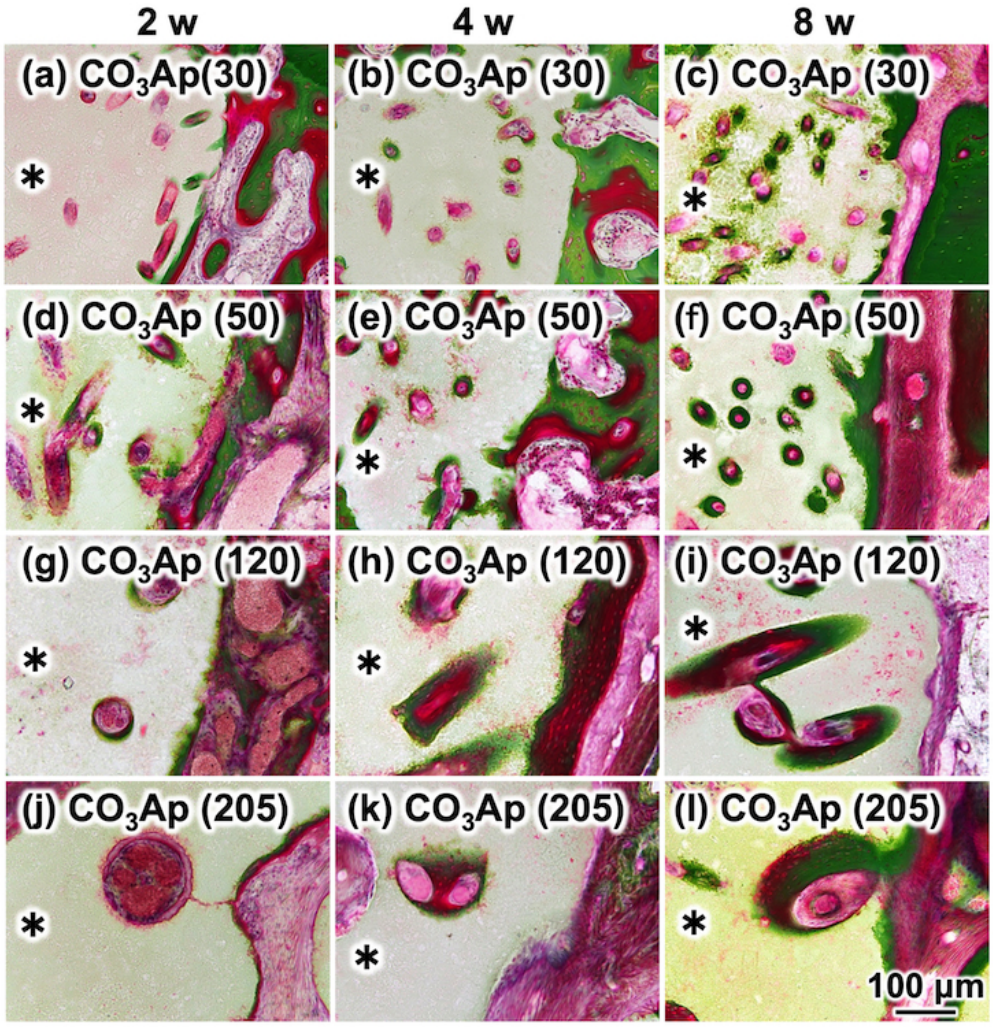

FIGURE 9. Typical higher-magnification histological images with Villanueva Goldner staining of (a, b, c) CO_3Ap (30), (d, e, f) CO_3Ap (50), (g, h, i) CO_3Ap (120), and (j, k, l) CO_3Ap (205) at 2, 4, and 8 weeks after implantation. (∗: CO_3Ap granule)

618x635mm (30 x 30 DPI)

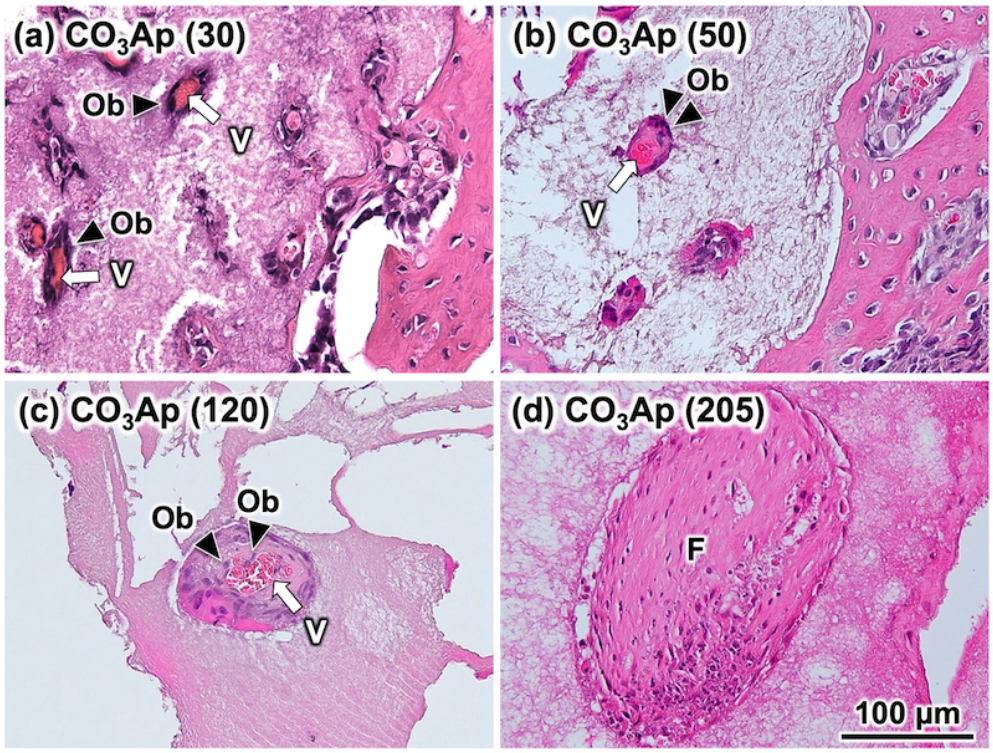

FIGURE 10. Typical histological images with hematoxylin and eosin staining of (a) CO_3Ap (30), (b) CO_3Ap (50), (c) CO_3Ap (120), and (d) CO_3Ap (205) at 2 weeks after implantation. (Ob: osteoblast, V: blood vessel, F: fibrous tissue)

681x516mm (30 x 30 DPI)

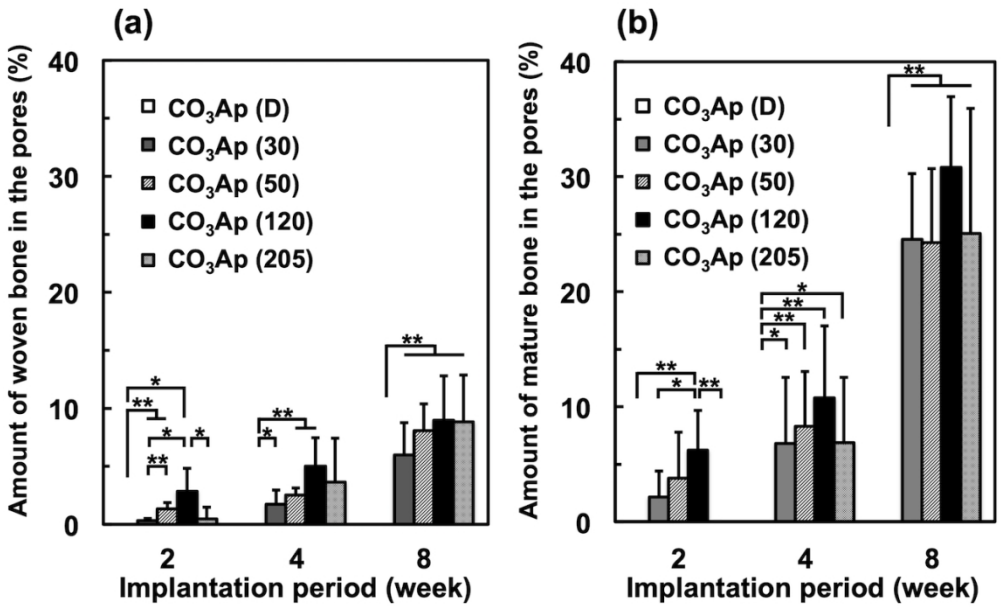

FIGURE 11. Percentage of new woven bone (a) and mature bone (b) in the pores of CO_3Ap granules at 2, 4, and 8 weeks after implantation (n = 5). (*p < 0.05, **p < 0.01)

843x511mm (40 x 40 DPI)

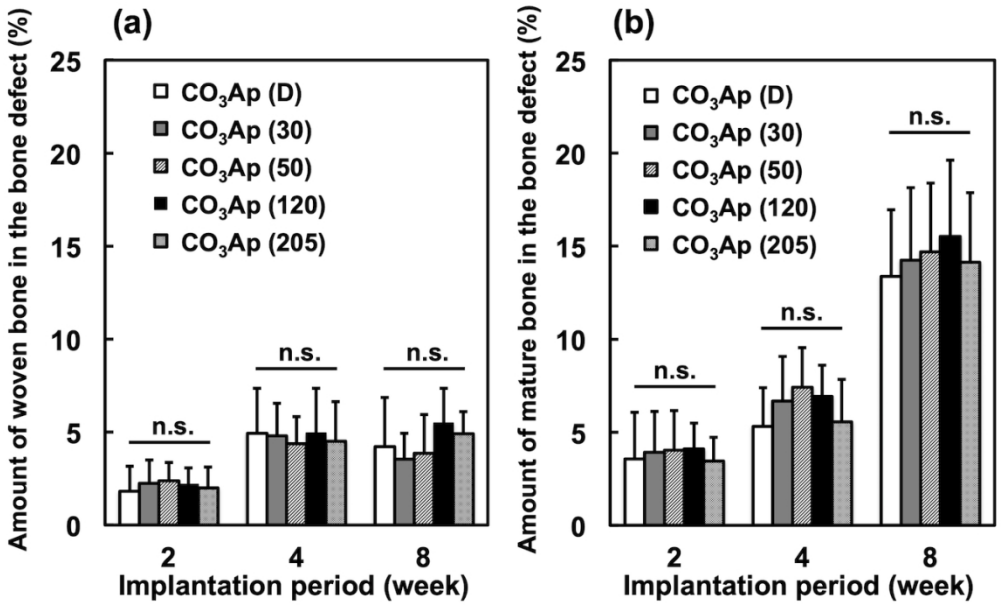

FIGURE 12. Percentage of new woven bone (a) and mature bone (b) in the whole bone defects reconstructed by porous CO_3Ap at 2, 4, and 8 weeks after implantation (n = 5).

846x510mm (40 x 40 DPI)

TABLE 1. Diameter of microfiber and pore size of porous $CaSO_4$, $CaCO_3$, and CO_3Ap granules, and reduction rate. Pore size was measured by SEM images.

Maker's description	Diameter (μm)			
	Original fiber	$CaSO_4$	$CaCO_3$	CO_3Ap
30 μm	32.8 ± 1.3	30.7 ± 1.7	28.8 ± 2.7	26.7 ± 1.1
50 μm	51.3 ± 1.8	48.7 ± 2.0	46.2 ± 1.8	44.8 ± 1.8
120 μm	124.8 ± 2.3	119.3 ± 1.8	116.5 ± 1.7	112.0 ± 1.6
205 μm	206.5 ± 2.8	197.0 ± 3.3	194.5 ± 2.9	189.5 ± 3.3
	Reduction rate (%)			
	Fiber to $CaSO_4$	$CaSO_4$ to $CaCO_3$	$CaCO_3$ to CO_3Ap	Fiber to CO_3Ap
30 μm	6.5 ± 5.6	5.9 ± 7.3	6.7 ± 9.6	18.7 ± 4.3
50 μm	5.2 ± 2.1	2.9 ± 6.0	4.9 ± 4.3	12.6 ± 2.3
120 μm	4.3 ± 1.7	2.3 ± 2.6	3.9 ± 2.5	10.3 ± 1.6
205 μm	4.6 ± 1.3	1.2 ± 2.4	2.5 ± 2.3	8.2 ± 2.0